Nuclear Engineering and Technology 49 (2017) 1079–1089

Contents lists available at ScienceDirect

Nuclear Engineering and Technology

journal homepage: www.elsevier.com/locate/net

Original Article

Safety analysis of nuclear containment vessels subjected to strong earthquakes and subsequent tsunamis

Feng Lin*, Hongzhi Li

Department of Structural Engineering, Tongji University, Shanghai 200092, China

ARTICLE INFO

Article history:
Received 1 July 2016
Received in revised form
27 February 2017
Accepted 31 March 2017
Available online 27 April 2017

Keywords:
Containment Vessel
Limit State
Seismic Performance
Tsunami

ABSTRACT

Nuclear power plants under expansion and under construction in China are mostly located in coastal areas, which means they are at risk of suffering strong earthquakes and subsequent tsunamis. This paper presents a safety analysis for a new reinforced concrete containment vessel in such events. A finite element method-based model was built, verified, and first used to understand the seismic performance of the containment vessel under earthquakes with increased intensities. Then, the model was used to assess the safety performance of the containment vessel subject to an earthquake with peak ground acceleration (PGA) of 0.56*g* and subsequent tsunamis with increased inundation depths, similar to the 2011 Great East earthquake and tsunami in Japan. Results indicated that the containment vessel reached Limit State I (concrete cracking) and Limit State II (concrete crushing) when the PGAs were in a range of 0.8–1.1*g* and 1.2–1.7*g*, respectively. The containment vessel reached Limit State I with a tsunami inundation depth of 10 m after suffering an earthquake with a PGA of 0.56*g*. A site-specific hazard assessment was conducted to consider the likelihood of tsunami sources.

1. Introduction

The next several decades will see rapid development of the nuclear industry worldwide. In total, 64 nuclear reactors are currently under expansion and under construction, most of which are located in Asia [1]. However, a considerable number of these nuclear reactors are located in earthquake-prone areas and along at-risk shorelines, which underlines the potential hazards posed by strong earthquakes and subsequent large tsunamis [2]. The latest evidence of how dangerous these hazards are was the Great East earthquake and tsunami that occurred on March 11, 2011 in Japan. An earthquake of magnitude M9.0 struck offshore of northeastern Japan and generated a mega tsunami with maximum heights of nearly 40 m. The tsunami devastated the east coast of Japan and triggered the Fukushima nuclear power plant (NPP) accident. More than 20,000 people were killed and 140,000 people were displaced.

The Fukushima NPP accident should not be regarded as a rare catastrophic combination of an earthquake and tsunami, because sufficient evidence contradicts this argument [3]. Similar risks also exist for NPPs in China, Korea, India, etc. As an example, Fig. 1 illustrates the active, under expansion, and under construction civilian nuclear sites located on the shorelines of mainland China. Strong earthquakes can occur near the Ryukyu trench, Manila trench, or in the Taiwan region. Based on hazard assessments, it is known that the magnitudes and focal depths of these earthquakes, and the local bathymetric conditions, are all suitable for triggering tsunamis [4,5].

Damage caused by hazards from exterior events, e.g., earthquakes, to nuclear reactors can be efficiently prevented by a robust reinforced concrete (RC) containment vessel. Previously, many efforts have been made to investigate the seismic performance of nuclear containment vessel by means of numerical and experimental studies. Various numerical models of containment vessels have been developed; these can be classified into at least three categories. The first category has been referred to as the lumped mass model, which is used to obtain the global displacement and acceleration responses along the containment vessel height [6–9]. The second is the finite element method-based model (FE model), which uses solid elements to discretize the RC containment vessels [10,11]. The third category is the FE model, which uses layered shell elements for concrete and imbedded rebar in the containment vessels [6,12]. Dynamic time history analysis has often been used in the three classified models with consideration of the material nonlinearity. Generally, the lumped mass models have the

* Corresponding author.
E-mail address: lin_feng@tongji.edu.cn (F. Lin).

http://dx.doi.org/10.1016/j.net.2017.03.008

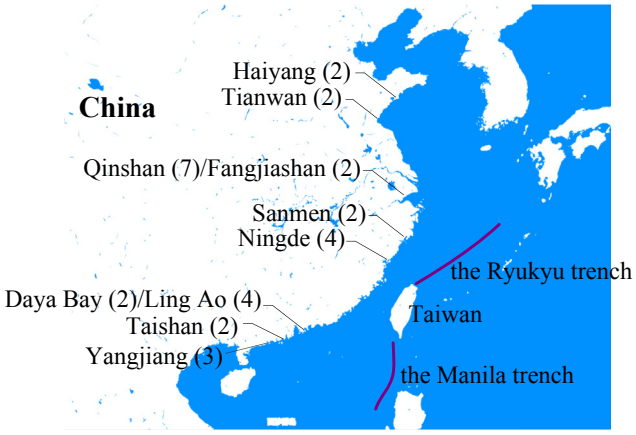

Fig. 1. Civilian nuclear sites with nuclear reactor number located on shorelines in mainland China, with some located in at-risk areas designed as subject to potential earthquakes and tsunamis.

advantage of computational efficiency. This has made a probabilistic analysis possible by investigating the seismic response of the containment vessels under a number of earthquake excitations. However, local responses, e.g., stress development and concrete cracking, were impossible to determine when using the lumped mass models. In these cases, with increased computational consumption, FE models using layered shell elements were applicable to gain integrated information both on levels of local regions and global structures. For the aspects of experimental studies, from 1992 to 1999, a 1:8-scale model of an RC containment vessel was tested on a shaking table at Tadotsu Engineering Laboratory in Japan [13–15]. One of the purposes of these studies was to verify the structural integrity of a containment vessel subject to design earthquakes. Results verified that the seismic safety margin was 5.8 times that of the design earthquake. Later, a pseudodynamic test was conducted on a 1:10 scale model using an unbonded prestressed concrete containment vessel [16]. Tests indicated that the containment vessel would remain elastic under US criteria for earthquake safe shutdown. Using these test data, a three-dimensional FE model using layered shell elements was developed to discretize the containment vessel and to perform a dynamic time history analysis [12]. Results confirmed that the stresses of the vertical and horizontal rebar were within the elastic limit throughout the earthquake excitation, with a horizontal peak ground acceleration (PGA) of 1.0*g*. This level of PGA was recorded at the MYG013 station during the 2011 Great East earthquake in Japan. Recently, a shaking table test using a 1:15-scale RC containment model was performed [17]. Results showed that the prototype containment was within the elastic range and had sufficient seismic safety margin under seismic motion, with a horizontal PGA of 0.25*g*.

Secondary tsunamis may be caused by a specific submarine earthquake. Most of the tsunamis in history have been generated by submarine earthquakes. When tsunami waves approach shorelines, they can break offshore depending on the coastal bathymetry. Subsequently, tsunami waves advance in a form of a hydraulic bore with a sudden increase in water level, resulting in impact effect on coastal structures. This effect can be described by several force components including: (1) hydrostatic force, (2) hydrodynamic force, (3) buoyant and uplift forces, (4) surge force, (5) debris impact, and (6) damming force [18–20]. A detailed comparison among the different codes in terms of individual force components can be found in the work of Palermo et al. [21], who also discussed various tsunami-induced load combinations. Kim and Kang [22] used numerical simulations to predict the maximum and minimum wave heights at the intake of the Ulchin NPP in Korea. It was found that almost all of the intake water pumps have a safety margin of more than 2 m, and the NPP site seems to be safe in the event of tsunamis.

Despite these efforts, limited information has been available on the safety assessment of nuclear containment vessels subjected to tsunamis, and even less information is available for cases of combined strong earthquake and subsequent tsunami. Meanwhile, a new RC containment vessel was developed for some of the generation III$^+$ NPPs on the shorelines of mainland China. However, the structural performance of this type of containment vessel, designed to resist earthquakes and tsunamis, has not been well investigated. In this regard, this paper presents a safety analysis of this advanced RC containment vessel subjected to strong earthquake and tsunami. The originality and significance of the study are addressed in the following aspects:

- The effect of the twin disasters on containment vessels was separated based on the sequence and interval of the events.
- Two Limit States, i.e., Limit States I and II, were proposed and used for the safety assessment of the RC containment vessels.
- The study results can improve the understanding of the risk of a targeted containment vessel subjected to strong earthquake and subsequent tsunami.

Twin disasters are not expected to occur simultaneously because the coastal structures experience them at different time intervals in nature. For example, in the cases of containment vessels in NPPs located on the mainland, shown in Fig. 1, fortunately, hypothetical tsunamis originate near the Ryukyu trench, Manila trench, or Taiwan region and propagate at a speed of about 700–800 km/h. As a result, tsunamis would take more than 2 h to land on the shorelines of mainland China after the occurrence of an earthquake [4,5]. In addition, a three-dimensional FE model of the containment vessel was built using the commercial program ANSYS/LS-DYNA [23] and a nonlinear time history analysis approach. This FE model made it possible to investigate the stress state of concrete in the containment vessel. After that, a static pushover analysis was implemented using the FE model to consider the containment vessel under influence of tsunami. Finally, safety assessments were conducted based on the analysis results.

2. FE model and model verification

2.1. Modeling of RC containment vessel

The targeted containment vessel primarily consists of an exterior RC containment vessel (also called a shield building), as shown in Fig. 2, and an interior steel containment vessel, which is not

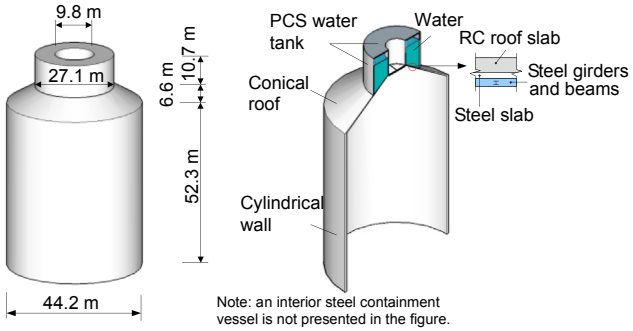

Fig. 2. Profile of the reinforced concrete (RC) containment vessel. PCS: passive containment cooling system.

presented in the figure. The total height of the exterior containment vessel is 69.6 m; the vessel mainly consists of a cylindrical wall, a conical roof, and a PCS (passive containment cooling system) water tank. The outer diameter of the cylindrical wall is 44.2 m; the wall thickness is 914 mm. The conical roof is composed of an upper RC roof slab and a lower steel supporting system to hold the PCS water tank located on the containment top. The steel supporting system includes 32 steel girders, connected beams, and an upper steel slab. The steel girders are arranged in a radial direction and connected by 15 beams in a circumferential direction. The function of the safety-related PCS water tank is to cool the nuclear reactor in the event of an accident. Thus, the tank is fully filled with water. The configuration of the interior steel containment vessel is not presented herein because it is relevant only for interior events, which are irrelevant to the exterior events involved in this study. A basement slab of 12 m thickness located at the bottom of the RC containment vessel is not shown in Fig. 2. Excluding the basement, the RC containment vessel approximately weighs 25,000 tons, including about 3,000 tons of water.

Fig. 3 illustrates the three-dimensional FE model of the RC containment vessel without the basement. The cylindrical wall including the upper RC roof slab in the conical roof was modeled using layered shell elements (SHELL163) owing to the computational efficiency of this method. This element has four nodes and both bending and membrane capabilities. Fifteen integration points through the element thickness were applied, and each layer represents a specific material, i.e., concrete, meridional reinforcing steel bars or circumferential reinforcing steel bars. The fractions of reinforcing steel bars in meridional and circumferential directions were specified by the design documents. The Belytschko–Tsay integration scheme was used because of its fast calculation speed and because it was recommended in [23]. The mesh size generally has a considerable effect on the accuracy of the numerical results. As is generally accepted, a model with finer meshing usually provides more reliable results but requires a longer computational time. Xu et al. [11] compared results for the natural frequencies of a similar RC containment vessel using mesh sizes of 0.2 m × 0.2 m, 2 m × 2 m, and 6 m × 6 m; they decided to use the 2 m × 2 m mesh size in their analysis. In this study, the mesh size was about 850 mm × 850 mm, which is considered reasonable compared to those with sizes of 2 m × 2 m and 1 m × 1 m in [11,24], which were both based on mesh-dependency analyses.

For modeling of the steel supporting system, the beam element (BEAM161) was adopted for the girders and beams using the conventional, compatible, and reliable Hughes–Liu integral algorithm with cross section integration. The shell elements (SHELL163) and beam elements (BEAM163) were perfectly connected via their common nodes. The tank was modeled using shell elements (SHELL163) incorporated in the conventional Lagrangian algorithm. The water in the PCS water tank was modeled using the solid elements (SOLID164) incorporated in an Arbitrary Lagrangian–Eulerian (ALE) algorithm, which made it possible to describe the fluid properties of water. A fixed boundary condition was adopted at the bottom of the RC containment vessel.

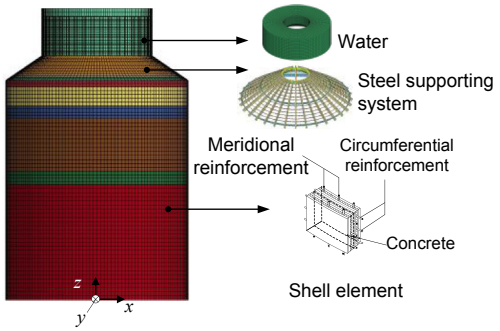

Fig. 3. Reinforced concrete (RC) containment vessel model.

The commonly used material model with the keyword "*MAT_CONCRETE_EC2" was applied for concrete and reinforcing steel bars in the containment wall [24]. Fig. 4 illustrates the stress–strain relationships for the concrete and reinforcing steel bars in the wall, which were subjected to loading, and unloading and reloading, under uniaxial compression and tension, respectively. Material equations governing the behavior of the concrete and reinforcing steel bars were taken from Eurocode 2 Part 1.2 [25]. The stress–strain relationships for concrete under axial compression and for reinforcing steel bars are expressed in Eqs. (1) and (2), respectively:

$$\sigma_c = \sigma_{c0} \times \left(\frac{\varepsilon_c}{\varepsilon_{c0}}\right) \times \frac{3}{2 + \left(\frac{\varepsilon_c}{\varepsilon_{c0}}\right)^3} \quad \text{for } \varepsilon_c < \varepsilon_{c0} \tag{1}$$

$$\sigma_s = \begin{cases} E_s \cdot \varepsilon_s & \text{for } \varepsilon_s < \varepsilon_{sy} \\ f_y & \text{for } \varepsilon_{sy} \le \varepsilon_s \le \varepsilon_{su} \end{cases}, \tag{2}$$

where σ_c and ε_c are the stress and strain of concrete under axial compression, respectively, and σ_{c0} and ε_{c0} denote the axial compressive strength and corresponding strain of concrete, respectively. A linear descending branch is adopted for concrete strain values exceeding ε_{c0} up to ultimate strain ε_{cu}. For the reinforcing steel bars, σ_s and ε_s are the stress and strain, E_s refers to the elasticity modulus, and f_y denotes yield strength; ε_{sy} and ε_{su} are the strain corresponding to f_y and the ultimate tensile strain, respectively. The axial compressive strength of concrete, σ_{c0}, was designed to be 27.6 MPa; and ε_{c0} and ε_{cu} were set at 0.0025 and 0.02, respectively. The yield strength f_y, elasticity modulus E_s, Poisson's ratio, and ultimate tensile strain ε_{su} of the reinforcing steel bars were set at 400 MPa, 2.0×10^5 MPa, 0.3, and 0.15, respectively. A softening effect for concrete under tension with axial tensile strength set at 2.2 MPa, plastic unloading for concrete under compression, and elastic unloading for concrete under tension were also considered. A plastic hardening kinematic model ("*MAT_PLAS-TIC_KINEMATIC") was used for the steel supporting system because this model is able to properly describe the hardening behavior of steel for the small strain cyclic loading involved in this study. The yield strength, elasticity modulus, Poisson's ratio, and effective plastic strain of the steel in the steel supporting system were empirically set at 350 MPa, 2.0×10^5 MPa, 0.3, and 0.2, respectively. In this paragraph, the strengths and elasticity moduli of materials were adopted from the design documents; other property parameters were used based primarily on common engineering experience. The Gruneisen equation of state was used to define the pressure, p, for water, with the parameter values taken from [11]:

$$p = \frac{\rho_0 c^2 \mu_0 \left[1 + \left(1 - \frac{\gamma_0}{2}\right)\mu_0 - \frac{\alpha}{2}{\mu_0}^2\right]}{\left[1 - (S_1 - 1)\mu_0 - S_2 \frac{{\mu_0}^2}{\mu_0 + 1} - S_3 \frac{{\mu_0}^3}{(\mu_0 + 1)^2}\right]^2} + (\gamma_0 + \alpha\mu_0)E, \tag{3}$$

where ρ_0 (1,000 kg/m^3) is water density; c (1,478 m/s) is the wave velocity; μ_0 (0) denotes the compression coefficient; γ_0 (0.11) refers to the Gruneisen coefficient; α (0) is the correction coefficient; S_1, S_2, and S_3 are three constants and have values of 1.979, 0, and 0, respectively; and E (0) is the initial intrinsic energy. The

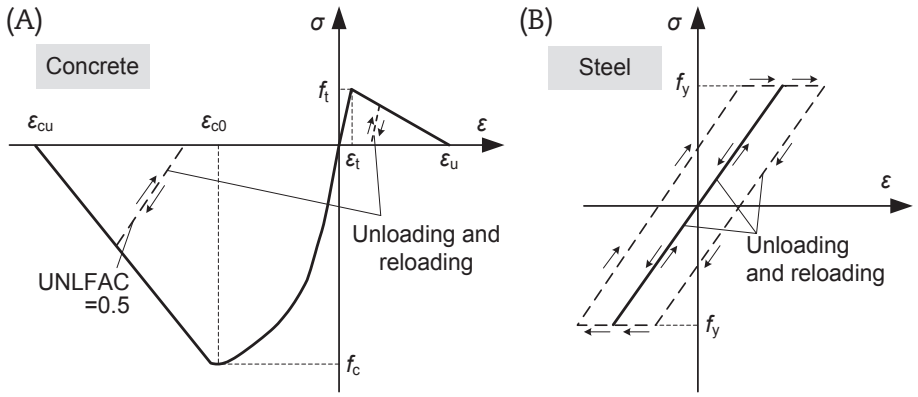

Fig. 4. (A) Stress-strain relationship for concrete. (B) Stress-strain relationship for reinforcing steel bars. Parameter UNLFAC controls unload stiffness and is adopted as 0.5.

fluid–structure interaction effect was achieved by defining the keyword CONSTRAINED_LAGRANGE_IN_SOLID and by using a coupling algorithm penalty function. Xu et al. [11] reported that tank water had a positive effect of limiting the vibration and efficiently dissipating the kinetic energy of the containment vessel because of the fluid–structure interaction.

In addition, the layered shell elements used a reduced integration scheme (i.e., the Belytschko–Tsay shell element), resulting in computational efficiency as well as undesired zero energy modes (hourglass modes). To control these hourglass modes, viscous damping was applied using the keyword "*HOURGLASS." The relevant parameters "Hourglass control type (IHQ)" and "Bulk viscosity type (IBQ)" were selected as the "Bulk viscosity type." The parameters "Hourglass coefficient (QM)," "Quadratic bulk viscosity coefficient (Q1)," and "Linear bulk viscosity coefficient (Q2)" were set at 0.10, 1.5, and 0.08, respectively, as suggested by Hallquist [23]. Generally, the hourglass is appropriately controlled when the hourglass energy is far less than the total internal energy. Fig. 5, in the form of a time history, illustrates the energy developed in block part 1 of the containment vessel under earthquake No. 1 (see Subsection 2.2). It was confirmed that the hourglass was well controlled.

Finally, prior to applying earthquake excitation, gravity force was loaded using the dynamic relaxation method; by setting the system damping coefficient to 0.0453784 during the first 10 s in computation, a sufficiently large damping was achieved. By doing this, numerical oscillation was avoided, which made this method possibly equivalent to static loading. After that, the natural periods of the RC containment vessel were investigated using an implicit method provided by the program LS-DYNA. The first and second natural periods, which are the primary contributors to structural responses under earthquakes, were close to each other by about 0.277 s owing to the central symmetry. It was possible to use the values of the natural periods to evaluate the duration of the earthquake waves, as shown in Subsection 2.2.

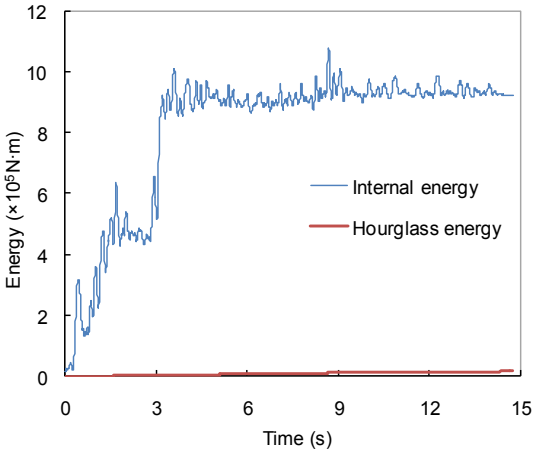

Fig. 5. Well control of hourglass for containment vessel under earthquake no. 1.

2.2. Input of earthquake waves

As is well known, input of appropriate earthquake waves is critical for a rational time history analysis of a structure. Generally, the PGA, time duration, and spectrum characteristics are the essential factors for the selection of earthquake waves. Table 1 presents seven earthquake waves used in this study. Their shear wave velocities in the site soils were larger than 700 m/s. Such values generally correspond to hard soil or rock, on which containment vessels are commonly sited. The time durations were considered to be sufficiently long compared to the basic period of the containment vessel (about 0.277 s).

An incremental procedure was used to obtain the earthquake intensities under which the containment vessel reached its Limit States (see Subsection 3.1). For each earthquake wave in Table 1, the PGA was first normalized, i.e., set to 0.05*g* in each of the two horizontal (*x* and *y*) directions and to 0.033*g* in the vertical (*z*) direction, with the ratio 0.05:0.033 = 1:0.66, in conformance with the Chinese code [26]. Then, each earthquake wave was imposed on the nodes of the bottom elements of the containment vessel to obtain the dynamic responses of the structure. If the containment vessel did not reach its Limit States, the PGA values in the *x* and *y* directions increased to 0.1*g*, 0.2*g*, 0.3*g*, etc., with a fixed step increment of 0.1*g*, until the Limit States of the containment vessel were finally reached. The PGA of each earthquake wave in the *z* direction was determined using the constant ratio of 0.66 to that in *x* and *y* directions.

Fig. 6 presents the acceleration response spectra (ARS) in the *x* direction of the seven earthquake waves and the standard ARS specified in the Chinese code [26]. Generally, the seven curves were close to the standard ARS curve. Similarity in curves was also observed for the earthquake waves in the *y* and *z* directions. The peaks of the acceleration responses of the seven earthquakes fell in an approximate range from 0.1 s to 0.2 s in the *x* direction and from 0.1 s to 0.3 s in the *y* direction. Obviously, the first and second natural periods (0.277 s) were near or within the peak range and could excite relatively large structural response under the selected earthquakes.

Table 1
Earthquake waves used in this study.

No.	Earthquake name	Station	V_s (m/s)	Peak ground accelerations (g)			Duration (s)
				x direction	*y* direction	*z* direction	
1	San Fernando	Cedar Springs	813.48	0.01963	0.01526	0.00953	14.7
2	Loma Prieta	Hayward City Hall—North	735.44	0.04887	0.05040	0.02757	39.4
3	Loma Prieta	UCSC Lick Observatory	713.59	0.46009	0.41676	0.37164	40.0
4	Northridge-01	LA-Wonderland Ave	1,222.52	0.10329	0.15899	0.10522	30.0
5	Whittier Narrows-01	Vasquez Rocks Park	996.43	0.06196	0.06585	0.03742	40.0
6	San Francisco	Golden Gate Park	874.72	0.08577	0.09532	0.03409	39.7
7	Coyote Lake	Gilroy Array#1	1,428.14	0.06331	0.09407	0.11663	26.9

For each earthquake wave in this table, peak ground acceleration was normalized and set to 0.05*g* in *x* and *y* directions, and to 0.033*g* in *z* direction.

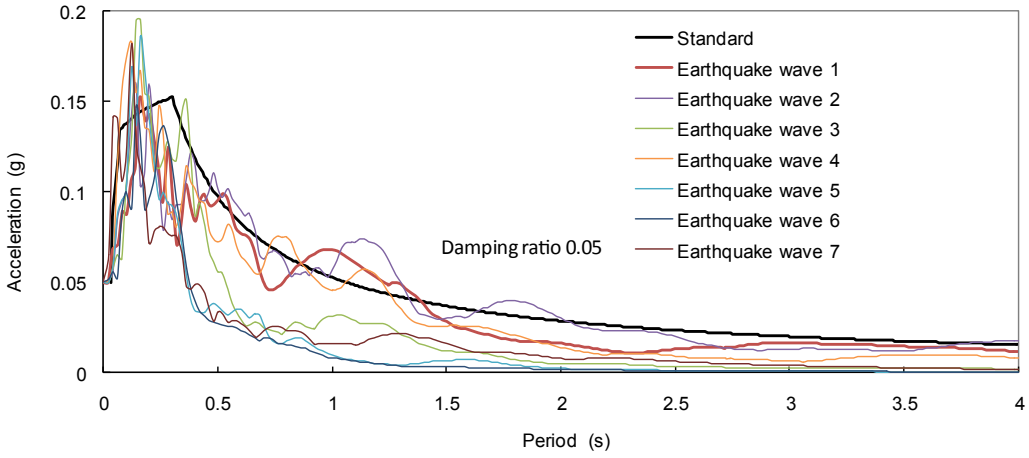

Fig. 6. Acceleration response spectra (ARS) in *x* direction for the seven earthquake waves and standard ARS specified in the Chinese code. From Standardization Administration of the People's Republic of China, Code for seismic design of buildings (GB50011-2010), Section 5, China Architecture & Building Press, Beijing, China, 2010. With permission.

2.3. Tsunami loads

A simplified model for tsunami loads was used in this study, with a consideration of the load components, load combinations, and parameter determination. First, the load components of hydrostatic force, hydrodynamic force, and surge force were considered as imposing on the containment vessel, whereas buoyant and uplift forces, debris impact, and damming force were ignored. This is because, physically, buoyant and uplift forces would not be generated in the case of a cylinder-like body attached close to the ground. Usually, nuclear containment vessels are located very close to the shoreline and directly face the sea. The possibility of impact from debris (e.g., floating driftwood, boats, automobiles, and building components) on containment vessels is small compared to the case of civil buildings.

The tsunami-induced load combination was considered to be "1.0 hydrostatic force + 1.0 surge force," with both partial factors adopted as 1.0 for the extreme events involved in this study. Fig. 7 presents a schematic tsunami loads–time curve related to the hydrostatic, hydrodynamic, and surge forces. The surge force is generally larger than the hydrodynamic force, and the two forces do not simultaneously load on structure surfaces [18,27]. The hydrostatic force and surge force can be expressed as Eqs. (4) and (5), respectively [18]:

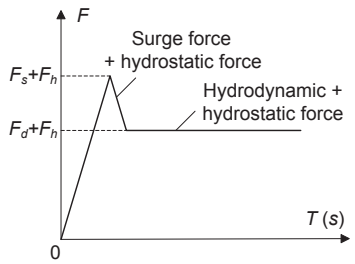

Fig. 7. Schematic representation of tsunami loads–time curve related to hydrostatic, hydrodynamic, and surge forces. F: tsunami loads, T(s): time in unit of second, F_s: the surge force, F_h: the hydrostatic force, F_d: the hydrodynamic force.

$$F_h = \frac{1}{2}\rho_S g b h_{\max}^2 \tag{4}$$

$$F_s = 1.5F_d = 1.5 \cdot \frac{1}{2}\rho_S C_d B\left(hu^2\right)_{\max}, \tag{5}$$

where F_h, F_d, and F_s are the hydrostatic force, the hydrodynamic force, and the surge force, respectively; ρ_s (1,200 kg/m^3) refers to the fluid density, including sediment and debris; g (9.81 m/s^2) denotes the gravitational acceleration; b is the breadth (width) of the body; h_{max} is the maximum inundation depth (i.e., water height above the containment base); C_d refers to the drag coefficient and is recommended to be set at 2.0 by the Federal Emergency Management Agency [18]; B denotes the breadth of the containment vessel in the plane normal to the flow direction; h is the inundation depth; and u is the flow velocity at the location of the containment vessel. For the calculation purposes of this study, b and B are equivalent. Note that the surge force F_s was simplified as a uniform static load along the containment height within the inundation depth. For the flow velocity u, the current estimates are crude [21]. Commonly, u can be calculated as:

$$u = C\sqrt{gh}, \tag{6}$$

where C is a constant coefficient and was assumed to be 2.0 in [18].

Foytong et al. [28] compared the results from previous studies and found the value of 2.0 to be conservatively large. They recommended that the appropriate value for coefficient C should range from 0.7 to 2.0. Unfortunately, a proper value of the coefficient C is currently not available. In this regard, an average value of 1.35 was adopted for coefficient C in this study.

Obviously, in Eqs. (5) and (6), hu^2 reaches its maximum value $(hu^2)_{max}$ when h is set to h_{max}. Thus, only one parameter, h_{max}, had to be determined in the model. The value of h_{max} refers to the scenario of the 2011 Great East earthquake and tsunami in Japan. The design inundation depth was 6 m; the recorded maximum inundation depth in the event was about 14–15 m [29]. In this regard, the parameter h_{max} was first adopted as 6 m and increased at an interval of 1 m until the containment vessel reached its Limit States.

Finally, Fig. 8 illustrates the approximate tsunami loading model used in this study. Both hydrostatic force and surge force were imposed on the surface of half of the containment cylinder in a radial direction. By doing this, the parameter B, which denotes the breadth of the containment vessel in the plane normal to the direction of flow, was appropriately calculated and found to be 44.2 m. As a result, the surge force was implicitly implemented.

2.4. Model verification

Shaking table tests of a containment vessel specimen were reported in [17,30] and were used to a certain extent to verify the developed model for the containment vessel. Fig. 9 illustrates information on the dimensions and reinforcement of the specimen, which was a 1:15 scaled RC containment vessel without application of prestress. The specimen was fabricated using microaggregate concrete and zinc-coated steel wires. The density, elasticity modulus, and Poisson's ratio were 2,300 kg/m^3, 6.5 × 10^3 MPa, and 0.2 for the microaggregate concrete, and 7,800 kg/m^3, 2.1 × 10^4 MPa, and 0.25 for the zinc-coated steel wires, respectively. The El Centro, the Taft, and an artificial earthquake waves were sequentially input as earthquake excitations in one horizontal direction. Acceleration and displacement gauges were installed at points P1, P2, P3, and P4, as illustrated in Fig. 9, to monitor the structural responses.

Following the approach described in Subsection 2.1, Fig. 10 presents the numerical model of the containment vessel specimen. The mesh size was about 70 mm × 70 mm for the shell and dome. For discretization of the basement, solid elements (SOLID164) and beam elements (BEAM161) were used for the microaggregate concrete and zinc-coated steel wires, respectively, with a mesh size of about 90 mm × 90 mm × 60 mm for concrete. The Johnson–Holmquist concrete model (*MAT_JOHNSON_HOLMQUIST_CONCRETE) and a plastic hardening kinematic model

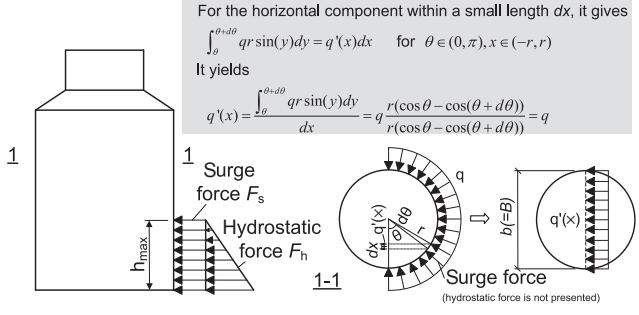

Fig. 8. Hydrostatic force and surge force applied to containment vessel. θ: angle, dθ: angle increment, y: angle variable, q: force in radial direction, q'(x): force in horizontal direction, r: radius, x: length form −r to r, dx: length increment, b: width.

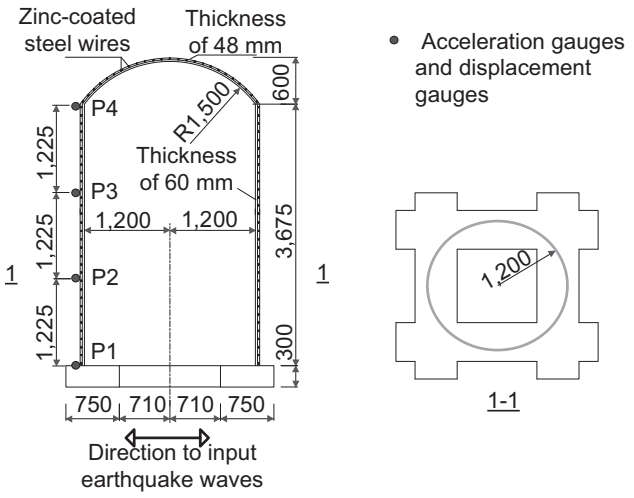

Fig. 9. Dimensions and reinforcement of containment vessel specimen on shaking table. P1, P2, P3, and P4: points to monitor structural responses.

Fig. 10. Numerical model of containment vessel specimen.

("*MAT_PLASTIC_KINEMATIC") were adopted for modeling the concrete and steel wires in the basement, respectively.

Table 2 compares the first 10 natural frequencies computed by Yuan [30] with those obtained from the proposed model. The errors were relatively small, varying from −7.78% to 0.50%. Table 3 compares the test and numerical results of structural responses for the containment vessel specimen under the El Centro earthquake, with PGAs of 0.1g, 0.2g, and 0.3g. The acceleration and displacement

Table 2
Comparison of first 10 natural frequencies.

No.	Natural frequency (Hz)		Error (%)
	Proposed model	Results in [30]	
1	15.114	14.918	1.30
2	15.114	15.038	0.50
3	19.893	19.716	0.90
4	19.894	19.772	0.62
5	23.547	23.888	−1.43
6	23.548	24.733	−4.79
7	32.216	32.844	−1.91
8	32.217	34.253	−5.94
9	36.822	38.911	−5.37
10	38.557	41.811	−7.78

Note: error = (result of proposed model result in [30])/result in [30].

Table 3
Comparison of structural responses of test and numerical results for containment vessel specimen under El Centro earthquake with PGAs of 0.1*g*, 0.2*g*, and 0.3*g*.

Point	Acceleration (*g*)									Displacement (mm)								
	Test results [17,30]			Numerical results			Error (%)			Test results [17,30]			Numerical results			Error (%)		
	0.1 *g*	0.2*g*	0.3*g*	0.1*g*	0.2*g*	0.3*g*	0.1*g*	0.2*g*	0.3*g*	0.1*g*	0.2*g*	0.3*g*	0.1*g*	0.2*g*	0.3*g*	0.1*g*	0.2*g*	0.3*g*
P4	0.167	0.285	0.402	0.160	0.299	0.425	4.19	4.91	5.72	−16.7	−30.8	46.0	−16.5	−29.4	42.4	1.15	4.66	7.85
P3	0.163	0.410	0.407	0.157	0.396	0.400	3.68	3.42	1.72	−16.8	−30.7	44.9	−16.5	−29.3	41.3	1.62	4.62	8.16
P2	0.146	0.240	0.369	0.142	0.230	0.388	2.74	4.17	5.15	−16.4	−30.4	45.0	−16.1	−29.0	41.3	1.84	4.49	8.27
P1	0.123	0.190	0.323	0.121	0.185	0.312	1.63	2.63	3.41	−16.1	−30.3	44.9	−15.9	−28.9	41.3	1.23	4.65	8.03

PGA, peak ground acceleration.

responses at points P1, P2, P3, and P4, obtained from the numerical model, were close to those of the test results, with errors ranging from 1.15% to 8.27% for displacement, and from 1.63% to 5.72% for acceleration. As a result, appropriate accuracy was achieved and the numerical model in Subsection 2.1 was properly verified to a certain extent.

3. Responses of containment vessel under earthquakes

3.1. Limit States

In the literature, various Limit States have been defined and used for safety assessment of RC containment vessels, such as the global yield of the primary reinforcing steel bars or the ultimate strength or strain limit of the material [31], the displacement on the containment top [7], the compressive damage index for concrete and the tensile damage index for steel [6], the maximum interstory drift ratio [32], and structural collapse [33], as well as tendon yielding and concrete crushing [12]. In essence, the variation in definitions reflects the complexity of the reasonable Limit State. In this study, two Limit States were proposed, i.e., Limit States I and II. Limit State I relates to concrete cracking, which is defined as the first principal strain (normally tensile principal strain) reaching 0.001, with a consideration of the strain-softening behavior of concrete under tension. This value was also used by Moon et al. [34], and recommended by the popular FE software Abaqus. Reaching Limit State I means concrete cracking has occurred across the containment thickness. Limit State II is associated with concrete crushing, which is defined as the third principal strain (normally compressive principal strain) reaching −0.0033. For concrete layers under plane stress condition in the containment wall, the ultimate compressive strain under biaxial loading changes slightly compared to that under axial compression, which was adopted as −0.0033 in accordance with the Chinese code [35]. Similar values of −0.003 and −0.0035 can be found in a textbook [36] and in an international code [37], respectively.

3.2. Computational results

Numerical results were presented in the form of strain contours at the two Limit States, at maximum displacement distribution and maximum acceleration distribution of the containment vessel in the *x* and *y* directions. Typically, for a containment vessel under earthquake Whittier Narrows-01, Figs. 11 and 12 illustrate the first principal strain distribution at Limit State I, and the third principal strain distribution at Limit State II, with maximum strain values of 0.001051 and −0.003598, respectively. The positions of the local regions reaching the two Limit States were not identical; however, both were close to the bottom of the containment vessel. Figs. 13 and 14 present the maximum acceleration and maximum displacement distributions of the containment vessel at different PGAs. Approximately linear increases of the displacement response

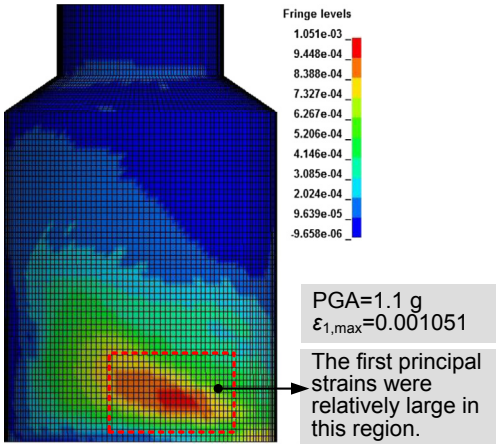

Fig. 11. First principal strain distribution of containment vessel concrete at Limit State I under earthquake Whittier Narrows-01. PGA, peak ground acceleration.

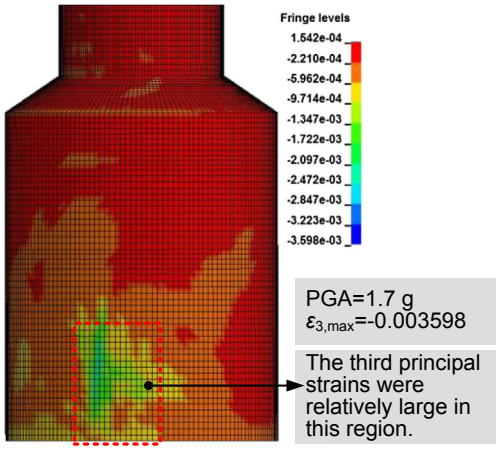

Fig. 12. Third principal strain distribution of containment vessel concrete at Limit State II under earthquake Whittier Narrows-01. PGA, peak ground acceleration.

were observed with increases of both the PGA of the earthquake and the containment vessel height. However, this observation is somewhat obscure for the maximum acceleration response mainly because of the plasticity development of concrete. Maximum accelerations also occurred on the containment top and were about 11*g* in the *x* direction and 7*g* in the *y* direction. Maximum displacements appeared on the containment top at about 60 mm in the *x* and *y* directions.

Table 4 summarizes the PGAs when the containment vessel reached Limit States I and II under individual earthquakes. For Limit State I, the PGAs ranged from 0.8*g* to 1.1*g*, whereas for Limit State II the PGAs varied from 1.2*g* to 1.7*g*. Evidently, a wide scatter of results

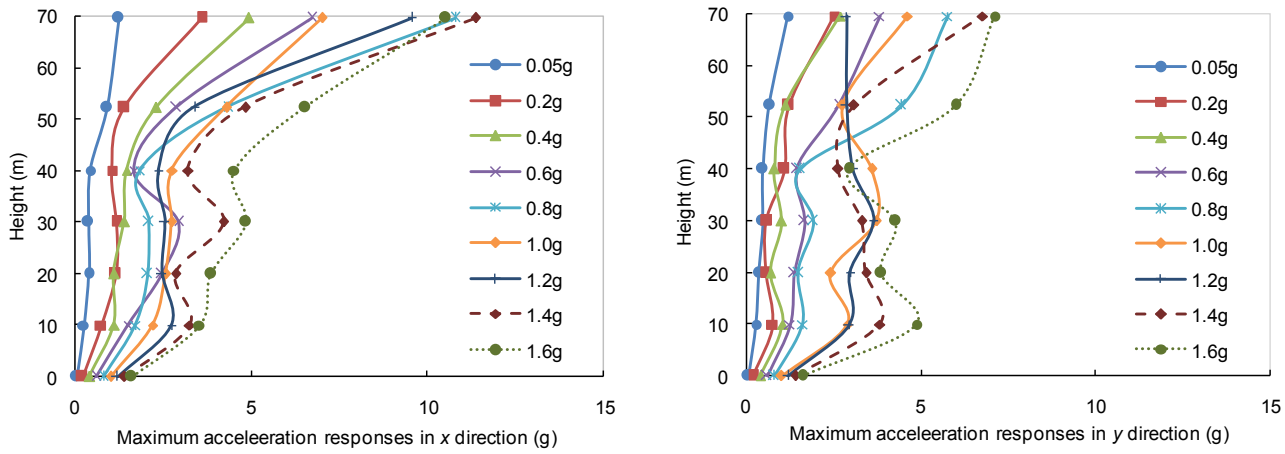

Note: results at PGAs of 0.1g, 0.3g, 0.5g, 0.7g, 0.9g, 1.1g, 1.3g, 1.5g and 1.7g are not presented in the figures for brevity.

Fig. 13. Maximum acceleration distributions of containment vessel at different peak ground accelerations (PGAs).

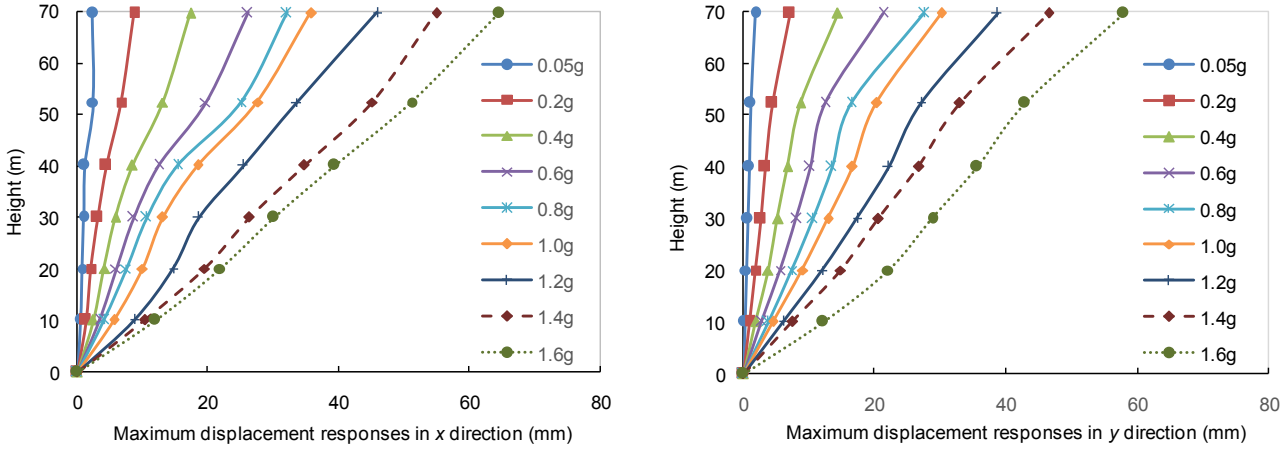

Note: results at PGAs of 0.1g, 0.3g, 0.5g, 0.7g, 0.9g, 1.1g, 1.3g, 1.5g and 1.7g are not presented in the figures for brevity.

Fig. 14. Maximum displacement distributions of containment vessel at different peak ground accelerations (PGAs).

Table 4
PGAs when the containment vessel reached Limit States I and II under individual earthquakes.

PGA (*g*)	Earthquake no.	
	Limit State I	Limit State II
0.8	2, 4	—
0.9	1, 3, 7	—
1.0	6	—
1.1	5	—
1.2	—	4
1.3	—	2, 3
1.4	—	1
1.5	—	7
1.6	—	6
1.7	—	5

Note: Earthquake no. refers to Table 1.
PGA, peak ground acceleration.

was found, which was consistent with the previous probabilistic analysis results [7,9]. Nevertheless, these results show that the PGAs were far beyond the safety level required to shut down nuclear reactors during earthquakes, which commonly takes place with a PGA of 0.25*g*. Finally, earthquakes associated with relatively large response in ARS (e.g., earthquake no. 2 as shown in Fig. 6) led to small PGAs when the containment vessel reached Limit States I and II.

4. Responses of containment vessel under successive earthquake and tsunamis

4.1. Computational assumptions

Three operational principles (assumptions) were adopted for a reasonable computation of the containment vessel under successive earthquake and tsunami. The first operational principle was that Earthquake No. 4 (Northridge-01) was used to perform the seismic analysis. The reason was that this earthquake wave led to the smallest PGA at Limit States I and II, as shown in Table 4 and, thus, was the most dangerous one among the seven earthquakes to impose on the containment vessel. The second operational principle was that a PGA of 0.56*g* was used for the seismic analysis. This value was recorded as the maximum PGA of the Unit 2 Daiichi reactor in the 2011 Great East earthquake in Japan. In addition, the

spatial distribution of PGA values showed that the coast near the Fukushima NPP (including the Daiichi reactor) was affected by PGAs of about 0.5*g* on average [29]. The third operational principle was that the inundation depth of the tsunami was originally set at 6 m and later increased at a fixed step of 1 m. In fact, the on-site design value for the inundation depth of the tsunami was 6 m and the recorded maximum inundation depth was about 14–15 m near Fukushima NPP during the event [29].

In summary, the containment vessel was first computationally attacked by the Northridge-01 earthquake, with a PGA of 0.56*g*. Approximately elastic responses were obtained and, thus, are not presented herein. After oscillating back to the stationary state, the containment vessel was subjected to the tsunami, with an inundation depth of 6 m, in accordance with the simplified model of tsunami load described in Subsection 2.3. The inundation depth increased at an interval of 1 m until Limit State I of the containment vessel was reached.

4.2. Computational results

Limit State I of the containment vessel was reached at an inundation depth of 10 m; the first (tensile) principal strain distribution is presented in Fig. 15. The maximum first principal strain reached 0.00111 at the bottom, which meant the concrete cracked across the containment thickness in that position. As expected, Limit State II was not yet reached and, thus, the third principal strain distribution of the containment vessel concrete was not present. The maximum tensile stress of the reinforcing steel bars in the containment wall was about 158 MPa, which was far less than their yield strength of 400 MPa. Fig. 16 illustrates the displacement distribution of the containment vessel at Limit State I. The maximum lateral displacement in the flow direction (about 3.9 mm) did not appear on the containment, but on the wall surface that directly resisted the tsunami water with a displacement value of 7.266 mm. This is because a slight concave formed there.

5. Safety assessments

The computational results of the structural responses indicated that the containment vessel would not reach Limit State I when experiencing the Northridge-01 earthquake with a PGA of 0.56*g* and subsequent tsunami with an inundation depth of no more than 10 m. Table 5 presents hazard assessments along the Chinese mainland coast in cases of hypothetical tsunamis [4,5]. Studies

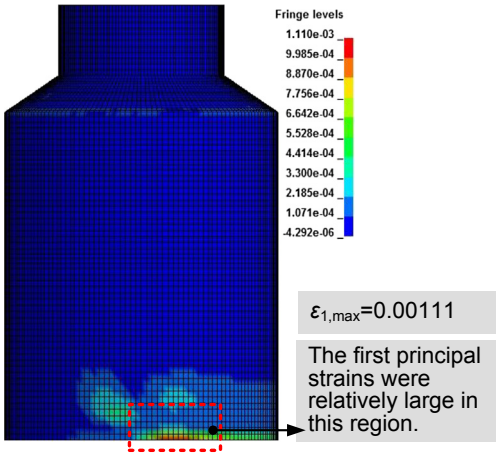

Fig. 15. First principal strain distribution of containment vessel at Limit State I under successive earthquake and tsunami.

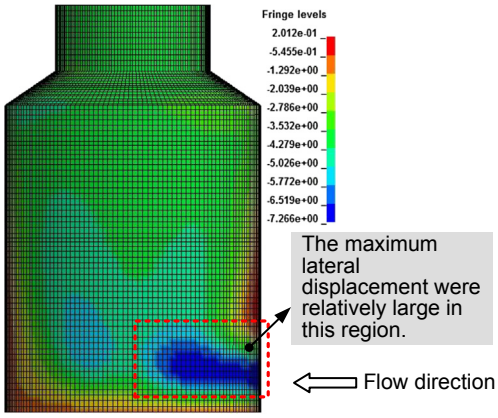

Fig. 16. Displacement distribution of containment vessel at Limit State I under successive earthquake and tsunami.

indicate that the maximum tsunami height would be about 3.3 m, far less than the hypothetical inundation depth of 10 m. The predicted earthquake epicenters on the surface were more than 500 km away from the nearest Chinese mainland coast. Such distances were far more than the distance of about 200 km, which was the case of the Daiichi nuclear reactor site in the 2011 Great East earthquake in Japan. Large distances mean that the arrival times of the tsunamis would be long and allow the nuclear reactors more time to take emergency measures. However, the magnitude of the 2011 Great East earthquake in Japan was M9, which is slightly stronger than some of the magnitudes listed in Table 5. It should be noted that, normally, earthquake-induced ground motion significantly attenuates with increase in distance between the earthquake source and the site. However, quantitative prediction of the attenuation amplitude in this case is difficult to provide because the attenuation additionally depends on the earthquake source and the site's geologic conditions [38]. Besides this, when tsunamis run up on shorelines, the maximum tsunami height is commonly less than the depth height owing to ground friction and the effects of obstacles such as buildings and trees. Generally, for the considered containment vessel used on the Chinese mainland coast, the structural performance is sufficiently strong under the conditions of suffering an earthquake with a maximum PGA of 0.56*g* and subsequent tsunami with an inundation depth of no more than 3.3 m.

Generally, safety assessments of the containment vessels involved in the two disasters can be separately analyzed. For a containment vessel subject to earthquake, the safety assessment can be performed based on the two Limit States. The seismic behavior of the structure is likely elastic with no residual stress, which is the case in this study. After that, structural analysis of the containment vessel under tsunami can be approximately implemented using a static pushover analysis. The associated safety assessment is conducted with consideration of the occurrence possibility, travel path, coastal bathymetry, etc.

6. Conclusions

NPPs located on the Chinese mainland coast are to be equipped with a new RC containment vessel. Safety assessment of the containment vessel when subjected to strong earthquake and subsequent tsunami was conducted. A validated three-dimensional FE model of the containment vessel was built and used to assess the seismic performance of the containment vessel under seven earthquakes; tests were conducted until the two predefined Limit

Table 5
Tsunami hazard assessment along the Chinese mainland coast.

Hypothetical tsunami source	Earthquake magnitude	Attacked areas	Maximum tsunami height (m)	Minimum arrival time (h)
Taiwan region [5]	M7.7–M8.2	Coast from Fujian Province to Zhejiang Province	3.3	≤3
Okinawa trench [4]	M9.0	Coast of Zhejiang Province	0.6	≤3
		Coast of Shanghai	0.15	7
Manila trench [4]	M9.0	Coast of south Taiwan	2.5	0.5
		Coast of Shanwei in Guangdong province	0.6	2.5
		Coast of Hong Kong	0.2	2.5

States were successively reached. Then, the containment vessel was subjected to a scenario similar to the event of the 2011 Great East earthquake and tsunami in Japan. Finally, a safety assessment of the containment vessel was conducted regarding site-specific tsunami hazards. Based on the study results, the following conclusions can be drawn:

(1) The containment vessel reached Limit State I (i.e., concrete cracking) when the PGAs of the earthquakes ranged from 0.8*g* to 1.1*g*, and reached Limit State II (i.e., concrete crushing) when PGAs of the earthquakes varied from 1.2*g* to 1.7*g*. These results were far beyond the safety shutdown requirements for containment vessels under earthquake, which are commonly set at a PGA of 0.25*g*.
(2) It was confirmed that, after suffering from an earthquake with a PGA of 0.56*g*, the containment vessel would not reach Limit State I unless the inundation depth of the tsunami was more than 10 m.
(3) Based on site-specific hazard assessment, for a hypothetical tsunami source generated in the Taiwan region, or in the Okinawa or Manila trenches, the structural performance was sufficiently strong to resist an earthquake with a maximum PGA of 0.56*g* and subsequent tsunami with an inundation depth of no more than 3.3 m.

The method of safety assessment presented in this paper can be generalized to any containment vessel under strong earthquake and subsequent tsunami. Further research can address probability analysis to obtain more reasonable results.

Conflicts of interest

All authors have no conflicts of interest to declare.

Acknowledgments

This research was sponsored by the National Science Foundation of China (Grant no. 51578399) and the National High-Tech Development Plan (Grant no. 2012AA050903).

Nomenclature

b	Breadth (width) of the body
B	Breadth of the containment vessel in the plane normal to the flow direction
c	Wave velocity
C	Constant coefficient for calculation of flow velocity u
C_d	Drag coefficient
E	Initial intrinsic energy
E_s	Elasticity modulus of reinforcing steel bars
F_d	Hydrodynamic force
F_h	Hydrostatic force
F_s	Surge force
f_y	Yield strength of reinforcing steel bars
g	Gravitational acceleration
h	Inundation depth
h_{max}	Maximum inundation depth
S_1, S_2, and S_3	Constants in Gruneisen state equation
u	Flow velocity at the location of the containment vessel
μ_0	Compression coefficient
α	Correction coefficient
σ_c	Tress of concrete under axial compression
γ_0	Gruneisen coefficient
ε_c	Strain of concrete under axial compression
ε_{c0}	Strain corresponding to σ_{c0}
ε_{cu}	Ultimate strain of concrete under axial compression
ε_s	Strain of reinforcing steel bars
ε_{sy}	Strain corresponding to f_y
ε_{su}	Ultimate tensile strain of reinforcing steel bars
ρ_0	Water density
ρ_s	Fluid density including sediment and debris
σ_{c0}	Axial compressive strength of concrete
σ_s	Stress of reinforcing steel bars

References

[1] International Atomic Energy Agency, IAEA Annual Report 2014, 2014. Vienna (Austria).
[2] C. Macilwain, Concerns over nuclear energy are legitimate, Nature 471 (2011) 549.
[3] F. Nanayama, R. Furukawa, K. Shigeno, A. Makino, Y. Soeda, Y. Igarashi, Unusually nine large tsunami deposits from the past 4000 years at Kiritappu marsh along the southern Kuril Trench, Sed. Geol. 200 (2007) 275–294.
[4] X. Zhao, H. Liu, B. Wang, Scenarios of local tsunamis in the China Seas by Boussinesq model, China Ocean Eng. 28 (2014) 303–316.
[5] J.M. Hou, X.J. Li, Y. Yuan, P.T. Wang, Tsunami hazard assessment along the Chinese mainland coast from earthquakes in the Taiwan region, Nat. Hazards 81 (2016) 1269–1281.
[6] H. Cho, H.M. Koh, C.H. Hyun, H.M. Shin, Seismic damage assessment of nuclear power plant containment structures, 13th World Conference on Earthquake Engineering, 2004. Vancouver, B.C. (Canada), Paper No. 2972.
[7] I.K. Choi, Y.S. Choun, S.M. Ahn, J.M. Seo, Probabilistic seismic risk analysis of CANDU containment structure for near-fault earthquakes, Nucl. Eng. Des. 238 (2008) 1382–1391.
[8] H. Lee, Y.C. Ou, H. Roh, J.S. Lee, Simplified model and seismic response of integrated nuclear containment system based on frequency adaptive lumped-mass stick modeling approach, KSCE J, Civ. Eng. 19 (2015) 1757–1766.
[9] T.K. Mandal, S. Ghosh, N.N. Pujari, Seismic fragility analysis of a typical Indian PHWR containment: comparison of fragility models, Struct. Saf. 58 (2016) 11–19.
[10] M. Manjuprasad, S. Gopalakrishnan, T.A. Rao, Non-linear dynamic response of a reinforced concrete secondary containment shell subjected to seismic load, Eng. Struct. 23 (2001) 397–406.
[11] Q. Xu, J. Chen, C. Zhang, J. Li, C. Zhao, Dynamic analysis of AP1000 shield building considering fluid and structure interaction effects, Nucl. Eng. Technol. 48 (2016) 246–258.
[12] A. Duan, Z. Zhao, J. Chen, J.R. Qian, W.L. Jin, Nonlinear time history analysis of a pre-stressed concrete containment vessel model under Japan's March 11 earthquake, Comput. Concr. 13 (2014) 1–16.
[13] T. Hirama, M. Goto, T. Hasegawa, M. Kanechikad, T. Keie, T. Miedaf, H. Abeg, K. Takiguchih, H. Akiyamai, Seismic proof test of a Reinforced Concrete Containment Vessel (RCCV): Part 1. Test model and pressure test, Nucl. Eng. Des. 235 (2005) 1335–1348.
[14] T. Hirama, M. Goto, K. Shiba, T. Kobayashid, R. Tanakac, S. Tsurumakie, K. Takiguchif, H. Akiyamag, Seismic proof test of a reinforced concrete containment vessel (RCCV): Part 2: Results of shaking table tests, Nucl. Eng. Design 235 (2005) 1349–1371.
[15] T. Hirama, M. Goto, H. Kumagai, Y. Naitod, A. Suzukie, H. Abef, K. Takiguchig,

H. Akiyamah, Seismic proof test of a reinforced concrete containment vessel (RCCV): Part 3. Evaluation of seismic safety margin, Nucl. Eng. Des. 237 (2007) 1128–1139.
[16] J.R. Qian, Z.Z. Zhao, A. Duan, Z.F. Xia, M.D. Wang, Pseudo-dynamic tests of a 1: 10 model of pre-stressed concrete containment vessel for CNP1000 nuclear power plant, J. China Civ. Eng. 40 (2007) 7–13 (in Chinese).
[17] X.L. Wang, G.L. Hou, D.G. Lv, Shaking table tests of a 1:15 reinforced concrete containment vessel model for nuclear power plant, Eng. Mech. 31 (2014) 249–252, 264. (in Chinese).
[18] U.S. Federal Emergency Management Agency, Guidelines for Design of Structures for Vertical Evacuation from Tsunamis (FEMA P646), Section 6, FEMA, Washington (DC), 2008.
[19] Department of Planning and Permitting of Honolulu Hawaii, City and County of Honolulu Building Code, Chapter 16, Article 11, 2000. Honolulu (HI).
[20] American Society of Civil Engineers/Structural Engineering Institute, Minimum Design Loads for Buildings and Other Structures (ASCE/SEI 7-16), Chapter 6, ASCE/SEI, 2016. Reston (VA).
[21] D. Palermo, I. Nistor, Y. Nouri, A. Cornett, Tsunami loading of near-shoreline structures: a primer, Can, J. Civ. Eng. 36 (2009) 1804–1815.
[22] J.Y. Kim, K.S. Kang, Assessment of the safety of Ulchin nuclear power plant in the event of tsunami using parametric study, Nucl. Eng. Technol. 43 (2011) 175–186.
[23] J.O. Hallquist, LS-DYNA Theory Manual. Livermore Software Technology Corporation, 2006. Livermore (CA).
[24] F. Lin, H. Ji, Y. Li, Z. Zuo, X. Gu, Y. Li, Prediction of ground motion due to the collapse of a large-scale cooling tower under strong earthquakes, Soil Dyn. Earthq. Eng. 65 (2014) 43–54.
[25] European Committee for Standardization, Design of Concrete Structures-part 1.2: General Rules—structural Fire Design, EN1992-1-2, Section 3, 2004. Brussels (Belgium).
[26] Standardization Administration of the People's Republic of China, Code for Seismic Design of Buildings (GB50011-2010), Section 5, China Architecture & Building Press, Beijing (China), 2010 (in Chinese).
[27] Y. Nouri, I. Nistor, D. Palermo, A. Cornett, Experimental investigation of tsunami impact on free standing structures, Coast Eng. J. 52 (2010) 43–70.
[28] P. Foytong, A. Ruangrassamee, P. Lukkunaprasit, N. Thanasisathit, Behaviours of reinforced-concrete building under tsunami loading, IES J, Part A: Civ. Struct. Eng. 8 (2015) 101–110.
[29] Iter Consult, Independent technical evaluation and review, Fukushima Daiichi nuclear accident first considerations, preliminary report [Internet], 2011 [cited 2016 Jun 13]. http://www.iter-consult.it/ITER_Report_Fukushima_Accident.pdf.
[30] Z.B. Yuan, Shaking Table Tests and Numerical Analysis for a Containment in Nuclear Power Plant, Harbin Engineering University, Harbin (China), 2012 (in Chinese).
[31] H.T. Tang, Q.A. Hossain, M.K. Ravindra, Containment capacity and failure modes for conditions beyond design basis, J. Energy Eng. 119 (1993) 101–118.
[32] American Society of Civil Engineers/Structural Engineering Institute, Seismic Design Criteria for Structural Systems, and Components in Nuclear Facilities (ASCE 43-05), Chapter 5, ASCE/SEI, Reston (VA), 2005.
[33] N.K. Prinja, D. Shepherd, J. Curley, Simulating structural collapse of a PWR containment, Nucl. Eng. Des. 235 (2005) 2033–2043.
[34] J. Moon, C.W. Roeder, D.E. Lehman, H.E. Lee, Analytical modeling of bending of circular concrete-filled steel tubes, Eng. Struct. 42 (2012) 349–361.
[35] Ministry of Housing and Urban–Rural Development of the People's Republic of China, Code for Design of Concrete Structures (GB50010-2010), Section 6.2, China Architecture & Building Press, Beijing (China), 2010 (in Chinese).
[36] J.K. Wight, J.G. MacGregor, Reinforced Concrete: Mechanics and Design, sixth ed., Pearson Prentice Hall, Upper Saddle River (NJ), 2005.
[37] CEB-FIP Model Code 2010, Part II, Section 5.1, Committee Euro-International du Beton, Lausanne (Switzerland), 2010.
[38] P. Gülkan, E. Kalkan, Attenuation modeling of recent earthquakes in Turkey, J. Seismol. 6 (2002) 397–409.